

Photo-induced nonequilibrium response in heavily underdoped $\text{YBa}_2\text{Cu}_3\text{O}_{6.45}$ probed by time-resolved terahertz spectroscopy

S. J. Zhang,¹ Z. X. Wang,¹ H. Xiang,² X. Yao,² Q. M. Liu,¹

L. Y. Shi,¹ T. Lin,¹ T. Dong,¹ D. Wu,¹ and N. L. Wang^{1,3,*}

¹*International Center for Quantum Materials,*

School of Physics, Peking University, Beijing 100871, China

²*School of Physics and Astronomy, Shanghai Jiao Tong University, Shanghai 200240, P. R. China*

³*Collaborative Innovation Center of Quantum Matter, Beijing, China*

Abstract

Intense laser pulses have recently emerged as a tool to tune between different orders in complex quantum materials. Among different light-induced phenomena, transient superconductivity far above the equilibrium transition temperature in cuprates is particularly attractive. Key to those experiments was the resonant pumping of specific phonon modes, which was believed to suppress the competing orders and induce superconducting phase coherence. Here, we present a comprehensive study of photo-induced nonequilibrium response in heavily underdoped $\text{YBa}_2\text{Cu}_3\text{O}_{6.45}$. We find that upon photo excitations, Josephson plasma edge in the superconducting state is initially removed accompanied by quasiparticle excitations, and subsequently reappears at frequency lower than the static plasma edge within short time. In the normal state, a much weaker edge-like shape is indeed induced by pump pulses in the reflectance spectrum and sustains even above room temperature. We compare the pump-induced effects between near- and mid-infrared excitations and exclude phonon pumping as a scenario for the above photo-induced effects. We further elaborate that the very weak edge structure is unlikely to be explained by photo-induced transient superconductivity.

High- T_c superconducting cuprates are highly anisotropic materials. The conducting CuO_2 layers are usually separated by insulating block layers, leading to insulator-like c-axis dc and optical responses in the normal state. The low frequency c-axis optical spectra of HTSC are dominated by the infrared active phonons with little contribution from free carriers. However, when the cuprate system goes into superconducting state, a very sharp plasma edge suddenly develops in the c-axis reflectivity spectrum. The plasma edge is caused by the condensed superfluid carriers via Josephson tunneling effect, which is referred to as Josephson plasmon¹⁻³. Manifestation of such c-axis Josephson plasma edge (JPE) is taken as an optical evidence for the occurrence of superconductivity.

Ultrashort pulses provide unique opportunities to manipulate different orders and physical properties in complex electronic materials. An unexpected finding is that intense ultrafast excitation can induce a Josephson plasma-like edge in normal state of cuprates, which was taken as an indication of light-induced transient superconductivity. The effect was first observed in a stripe-ordered cuprate $\text{La}_{1.8-x}\text{Eu}_{0.2}\text{Sr}_x\text{CuO}_4$ at 10 K whose T_c is less than 2 K⁴, then in underdoped $\text{YBa}_2\text{Cu}_3\text{O}_{7-\delta}$ at temperature even above room temperature^{5,6}. In those measurements, the pump excitation wavelength is tuned to about 15 μm (~ 20 THz) in mid-infrared (MIR) region which is assumed to be resonant with specific phonon modes of oxygens (e.g. in-plane Cu-O stretching mode or apical oxygen mode relative to CuO_2 planes). The resonant pumping of specific phonon mode is believed to be the key for light-induced superconductivity. The observations also motivated theoretical studies on transient superconductivity along the direction of the resonant phonon pumping⁷⁻¹³.

Near-infrared (NIR) pump was also used to investigate the photoexcitation induced effect in cuprates. Nicoletti et al. reported a surprisingly large effect on $\text{La}_{1-x}\text{Ba}_x\text{CuO}_4$ ($x=0.115$) sample: a blue shift of Josephson plasmon frequency with even enhanced edge amplitude for $T < T_c$, and a light-induced edge for $T > T_c$ in the stripe ordered state whose amplitude is comparable with that seen in the equilibrium superconducting state^{14,15}. Significant NIR pump-induced effect was recently also observed in time resolved THz measurement on other compositions of $\text{La}_{1-x}\text{A}_x\text{CuO}_4$ ($\text{A}=\text{Ba}, \text{Sr}$) and electron-doped $\text{Pr}_{1-x}\text{LaCe}_x\text{CuO}_4$ ¹⁶⁻²⁰. Those results are notably different from the above reports on $\text{La}_{1.8-x}\text{Eu}_{0.2}\text{Sr}_x\text{CuO}_4$ ⁴ and $\text{YBa}_2\text{Cu}_3\text{O}_{6.5}$ ^{5,6}, where the relative change of reflectivity is less than 20% even after taking the penetration depth mismatch into account. Nonetheless, up to now there is no report about c-axis terahertz measurement on $\text{YBa}_2\text{Cu}_3\text{O}_{7-\delta}$ driven by NIR pulse excitations.

Motivated by solving the discrepancies in different measurements, here we present a compre-

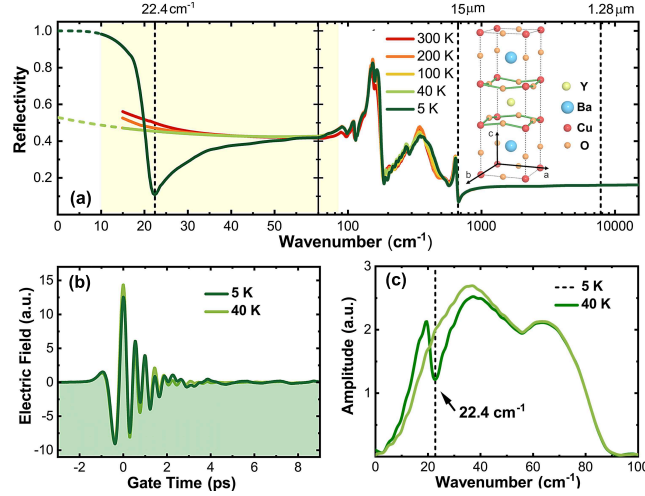


FIG. 1. Broadband reflectivity spectra $R(\omega)$ of $\text{YBa}_2\text{Cu}_3\text{O}_{6.45}$ along c -axis. (a) The out-of-plane reflectance spectra of YBCO behave in an insulating manner in normal state and are governed by phonons in FIR region. In superconducting state, two Josephson plasmon edges can be observed near 22.4 cm^{-1} and 500 cm^{-1} . Inset: $\text{YBa}_2\text{Cu}_3\text{O}_{7-\delta}$ contains two CuO_2 planes in a unit cell, leading to two longitudinal Josephson coupling modes with different coupling strengths. (b) reflected THz electric field $\tilde{E}_0(t)$ measured by a time domain THz spectroscopy system. (c) amplitude of Fourier transformation of $\tilde{E}_0(t)$, i.e. $|\tilde{E}_0(\omega)|$. Reflectivity at 5 K in the shaded area in (a) can be calculated with those values as presented in Appendix B.

hensive NIR and MIR pump, c -axis terahertz probe measurement on an underdoped $\text{YBa}_2\text{Cu}_3\text{O}_{6.45}$ (YBCO) superconductor with $T_c=35 \text{ K}$. We aim at addressing two critical issues with respect to the photo-induced effect in cuprates, that is, whether the phonon pumping is essential in inducing the effect, and whether the induced edge-like effect in reflectance spectrum could be unambiguously attributed to transient superconductivity? We elaborate that the present study does not favor positive answers to those questions.

Details of sample growth and spectral measurements are presented in Appendix A. Figure 1 (a) shows the broadband reflectivity spectra $R(\omega)$ of YBCO along c -axis, which was measured by Fourier transform infrared spectrometers (Bruker 113v and Vertex 80v) in combination with a time domain THz spectroscopy system. Similar to the previous results reported on the same doping level²¹, the out-of-plane spectra behave in an insulating manner, with low reflectivity governed by phonons in FIR region. Among all those phonons, the one locates near 650 cm^{-1} , which is assigned as an A_{2u} mode involving the bonds between apical oxygens and copper atoms²², has been drawing increasing attention for it may be related to the enhancement of superconductivity in

YBa₂Cu₃O_{7- δ} ²³. In the out-of-plane spectra, the appearance of longitudinal JPE reflects Josephson tunneling of Cooper pairs along c-axis. YBa₂Cu₃O_{7- δ} is a specific case of bilayer cuprates containing two different kinds of blocking layers, as illustrated in the inset of Fig. 1 (a). As a result, two longitudinal Josephson coupling modes with different coupling strengths can be observed in the out-of plane $R(\omega)$. The one near 22.4 cm⁻¹ comes from the coupling between pairs of CuO₂ layers in neighboring unit cells and the other near 500 cm⁻¹ from that in the same unit cell. With reasonable extrapolations (plotted as green dash lines in Fig. 1 (a)), all optical constants in such a broad range can be obtained through Kramers-Kronig transformation. In our pump-probe experiments, two selective pump wavelength are used to interrogate the pump-induced change in THz regime. MIR pump pulses are tuned to 15 μ m (667 cm⁻¹) in order to resonant with the phonon near 650 cm⁻¹, and NIR pump pulses are set to 1.28 μ m (7810 cm⁻¹) whose energy scale is notably higher than all the phonons and collective modes in YBCO.

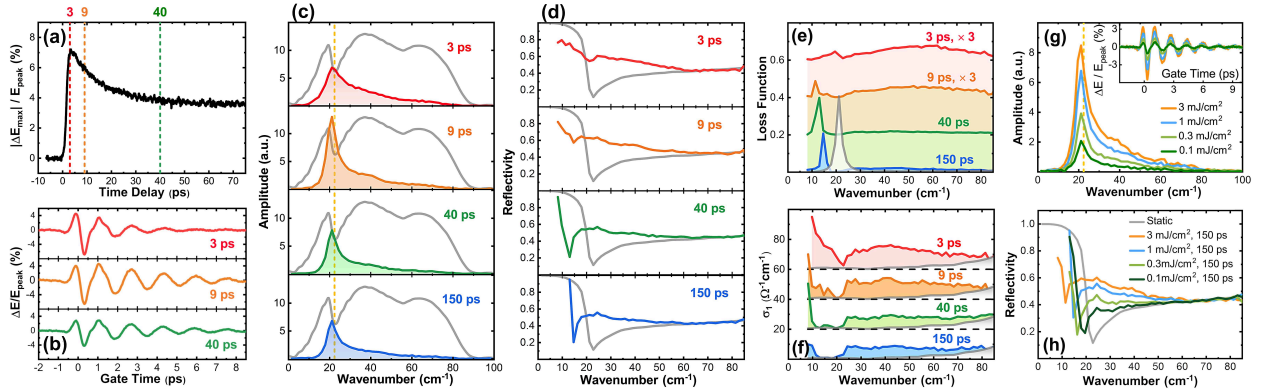


FIG. 2. Pump-induced changes after exciting by 1.28 μ m at 5 K. (a) the decay procedure of the maximum value of pump-induced change of the reflected THz electric field, $|\Delta E_{max}|/E_{peak}$, after excited by a fluence of 1 mJ/cm². E_{peak} is the maximum value of $\tilde{E}_0(t)$ at static position. (b) the pump induced relative change $\Delta \tilde{E}(t, \tau)/E_{peak}$ in time domain at three different time delays (labeled as dashed lines in (a)). (c) the Fourier transformed spectrum of $\Delta \tilde{E}(t, \tau)$. Grey lines is the Fourier transformation of static reflected electric field divided by a coefficient 4. (d) transient reflectivity (e) energy loss function $\text{Im}(-1/\epsilon(\omega))$ (f) conductivity. (g) fluence dependence of the pump-induced change of reflected electric field at 150 ps in time (inset) and frequency domain. (h) fluence dependence of transient reflectivity. Optical constants in static state are plotted in grey lines.

We now present NIR pump-induced change in THz regime in the superconducting state first.

Figure 2 (a) displays the decay procedure of the maximum absolute value of pump-induced change, $|\Delta\tilde{E}_{max}|/E_{peak}$, after excitation at $1.28 \mu\text{m}$ by a fluence of 1 mJ/cm^2 . Roughly a 7% maximum relative change is seen at 3 ps after excitation (red dash line). Then the signal decays by nearly half within 40 ps before reaching a metastable state. We define the time zero at the position where $|\Delta\tilde{E}_{max}|/E_{peak}$ starts to change. Figure 2 (b) shows the pump induced relative change $\Delta\tilde{E}(t, \tau)/E_{peak}$ in the superconducting state at several different time delays. At $\tau = 3 \text{ ps}$, i.e. the maximum position of $|\Delta\tilde{E}_{max}|/E_{peak}$, a fast-damping oscillation displays. An oscillation can be observed unambiguously at $\tau = 9 \text{ ps}$, with the oscillating period around 1.5 ps, accompanied by the decay of $|\Delta E_{max}|/E_{peak}$. Both $|\Delta E_{max}|/E_{peak}$ and the oscillation get attenuated at $\tau = 40 \text{ ps}$. Figure 2 (c) shows the amplitude of Fourier transformation of $\Delta\tilde{E}(t, \tau)$, i.e. $|\Delta\tilde{E}(\omega, \tau)|$. The clear oscillations of pump-induced THz signal in time domain gives a pronounced peak slightly below 22.4 cm^{-1} in frequency domain. $|\Delta\tilde{E}(\omega, \tau)|$ behaves quite differently compared with the static reflected electric field of THz $|\tilde{E}_0(\omega)|$ (plotted in grey lines), in which the pronounced peak suggests that the pump-induced change occurs predominantly near the static JPE position.

A multilayer model is used to obtain the authentic pump-induced change of optical properties, which is disguised by the non-negligible mismatch of the penetration depth of pump and probe pulses. The detailed calculation method and rationality of the model are presented in Appendix C. All the transient optical constants shown below are calculated with the multilayer model.

Figure 2 (d) shows the transient reflectivity at selective time delays. At the maximum position of pump-induced signal, i.e. at 3 ps, the transient reflectivity seems like a gentle slope with a slight dip near 22.5 cm^{-1} , with reflectivity below static JPE being suppressed and that above JPE being enhanced. The depression of static JPE indicates the breakdown of Josephson tunneling along c-axis. The enhancement of reflectivity indicates the excitation of quasiparticles. A tiny edge reappears at lower energy scale at 9 ps. Then the edge gets sharper at the subsequent time delays and turn to move to higher energy scale. This procedure is the recovery of Josephson tunneling after the excitation. An uplift above the static Josephson plasmon edge position can be seen in all the time delays with only slight decay, which is identified as the excitation of incoherent quasiparticles as being further explained below.

The depression and recovery procedure of Josephson plasmon mode after excitation can be seen more clearly in the evolution of peaks in energy loss function $\text{Im}(-1/\epsilon(\omega))$, as shown in Fig. 2 (e). In the static state, the JPE in reflectivity corresponds to a peak in energy loss function, plotted in grey lines. Upon exciting, the height of the peak is severely suppressed and the peak re-

emerges in lower energy scale after 9 ps. It deserves to mention that a broad bump at higher energy scale appears after excitation. In single-layer cuprates with only a uniform Josephson plasmon mode, a new longitudinal Josephson plasmon mode appears after excitation at $1.28 \mu\text{m}$ ^{16,17} as a new-emerging peak in energy loss function. But it seems not that case in YBCO for the bump is widespread without a specific energy scale. The development of broad feature is also clearly seen in $\sigma_1(\omega)$, as shown in Fig. 2 (f). The spectral weight of the broad feature is highest when $|\Delta E_{\text{max}}|/E_{\text{peak}}$ has the highest signal (i.e at 3 ps) but drops with time delays. A gap-like suppression is seen below the energy scale of JPE. It implies that the excited quasiparticles are still confined in the ab-plane and the c-axis coherence can not be established due to the insulating block layers. The binding energy has the energy scale of Josephson coupling strength. Therefore, the broad spectral feature could be interpreted as the excitation of incoherent quasiparticles. Figure 2 (g) and (h) show the fluence dependence of the pump-induced effects at 150 ps. With increasing pump fluence, Josephson plasmon edge is suppressed to lower energy scale and the excitation of quasiparticles gets more pronounced, which supports the scenario that pump pulses turn to deplete Josephson tunneling along c-axis and excite incoherent quasiparticles.

Figure 3 summarizes the NIR pump-induced change of YBCO normal state. There are three essential differences in the photo-induced change of reflected electric field in normal state compared with that in superconducting state. Firstly, the rise and decay time of $|\Delta E_{\text{max}}|/E_{\text{peak}}$ is relatively short in normal phase as shown in Fig. 3 (a). In normal state of YBCO, $|\Delta E_{\text{max}}|/E_{\text{peak}}$ rises to maximum position at 1.5 ps and decay to a metastable state within 10 ps. In contrast, it takes 3 ps for $|\Delta E_{\text{max}}|/E_{\text{peak}}$ in superconducting state to reach its maximum and over 40 ps to stabilize. The shorter rising time might be related to the melting of charge density wave order in underdoped cuprates^{24,25}. Secondly, the pump-induced change of reflected electric field is significantly smaller in normal phase compared with that in superconducting state at the same pump fluence, which is 1.3% and 8.2%, respectively. Thirdly, the damped oscillation with an oscillation period of 1.5 ps observed in the superconducting state at 5 K disappears completely in the pump-induced change $\Delta \tilde{E}(t, \tau)$, and the time duration of $\Delta \tilde{E}(t, \tau)$ is only 3 ps in normal phase, as shown in Fig. 3 (b). Figure 3 (c) shows the amplitude of Fourier transformation of $\Delta \tilde{E}(t, \tau)$, $|\Delta \tilde{E}(\omega, \tau)|$, which covers nearly all the THz regime generated in our experiments. $\Delta \tilde{E}(t, \tau)$ is multiplied by a Blackman window function before doing Fourier transformation to reduce the noise effect, which will not affect the calculated transient optical constants. Figure 3 (d) shows the calculated transient reflectivity at 1.5 ps after the excitation at $1.28 \mu\text{m}$ by a fluence of 3 mJ/cm^2 at the temperature of 40 K, which

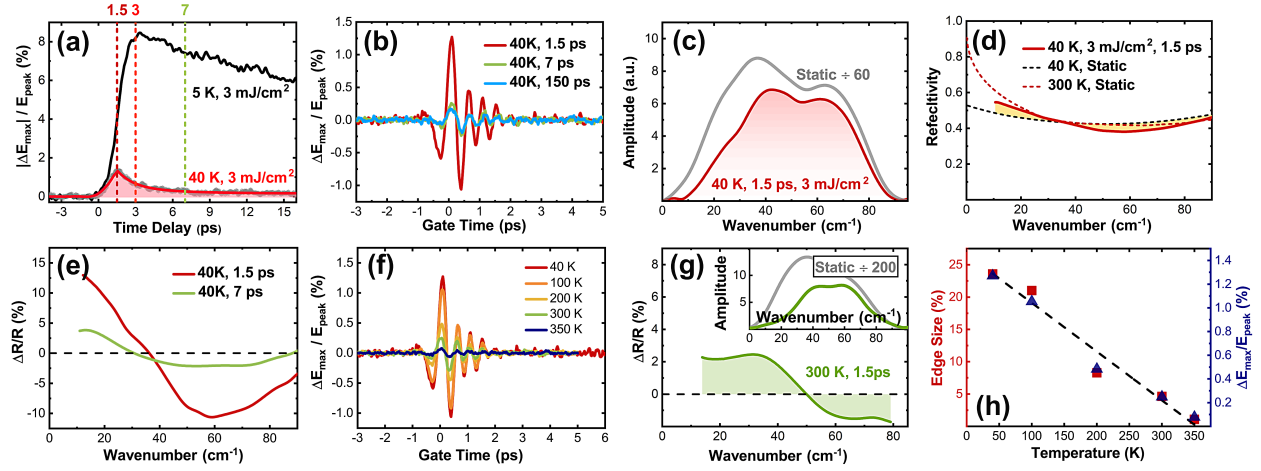


FIG. 3. Pump-induced changes after excitation at $1.28 \mu\text{m}$ by a fluence of 3 mJ/cm^2 in normal state. (a) the decay procedure of the maximum value of pump-induced change of the reflected THz electric field, $|\Delta E_{\text{max}}|/E_{\text{peak}}$, at 40 K (experimental results are plotted in grey dots, and the red line is guide for the eyes) and 5 K (black line). (b) the pump induced relative change $\Delta \tilde{E}(t, \tau)/E_{\text{peak}}$ in time domain at three different time delays. (c) the Fourier transformed spectrum of $\Delta \tilde{E}(t, \tau)$. Grey lines is the Fourier transformation of static reflected electric field divided by a coefficient, 60. (d) the transient reflectivity at 1.5 ps. Dashed lines are the static reflectivity at 5 K and 300 K for comparison. (e) the relative change of transient reflectivity at 40 K. (f) the temperature dependence of pump induced relative change $\Delta \tilde{E}(t, \tau)/E_{\text{peak}}$. (g) the relative change of transient reflectivity at 300 K. Inset: the Fourier transformed spectrum of static (grey) and transient change (green) of reflected THz electric field. (h) the edge size of transient reflectivity (calculated with the multilayer model, defined in the main text) and $|\Delta E_{\text{max}}|/E_{\text{peak}}$ ($\tau = 1.5 \text{ ps}$) are both linearly dependent with temperature.

represents the most significant photo-induced change. And the static reflectivity at 40 K and 300 K are also plotted in dashed lines for reference. A slight enhancement at lower energy scale and suppression at higher energy scale in transient reflectivity can be seen in transient $R(\omega, 1.5 \text{ ps})$, which is not in coincidence with reflectivity at 300 K so the heating effect of pump pulses can be excluded. Figure 3 (e) shows the relative change of transient reflectivity $\Delta R(\omega, 1.5 \text{ ps})/R(\omega)$ at two different time delays. The pump-induced signal $|\Delta E_{\text{max}}|/E_{\text{peak}}$ survives even above room temperature, 350 K, as shown in Fig. 3 (f). There is no essential difference between $\Delta R(\omega, 1.5 \text{ ps})/R(\omega)$ at 300 K (Fig. 3 (g)) and that at 40 K (Fig. 3 (e)) except for the magnitude. Temperature dependence of $|\Delta E_{\text{max}}|/E_{\text{peak}}$ and "edge size" of the edge-like shape (the difference between the maximum and

minimum of $\Delta R(\omega, 1.5ps)/R(\omega)$ are shown in Fig. 3 (h). Both those values are almost linearly dependent with temperature without showing any specific phase transition point.

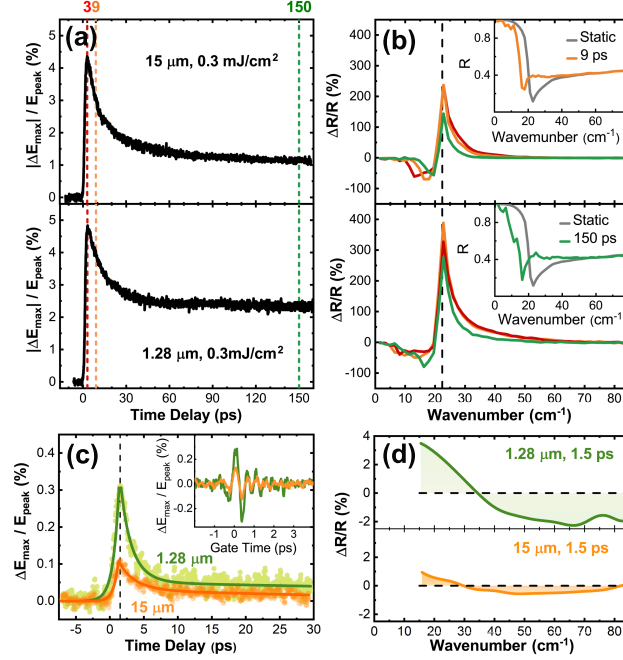


FIG. 4. Comparison between the pump-induced effects after the excitation of 15 μm and 1.28 μm pulses at 0.3 mJ/cm². (a) the decay procedure of the maximum value of pump-induced change of the reflected THz electric field, $|\Delta E_{max}|/E_{peak}$ at 5 K. (b) the pump-induced relative change of reflectivity at 5 K. (c) the decay procedure of the maximum value of pump-induced change of the reflected THz electric field, $|\Delta E_{max}|/E_{peak}$ at 40 K. (d) the pump-induced relative change of reflectivity at 40 K.

We also performed MIR pump-THz probe experiments on YBCO in superconducting and normal states as shown in Fig. 4, in which the MIR pump pulses are tuned to 15 μm , resonating with the apical-oxygen-related phonon. The rise and decay procedure of $|\Delta E_{max}|/E_{peak}$ is exactly the same after the excitation of MIR and NIR pump pulses, no matter in superconducting and normal phase, as shown in the left panel of Fig. 4. For MIR pump, $|\Delta E_{max}|/E_{peak}$ decays to the metastable state with relatively smaller value compared with NIR pump, which may result from less quasiparticles excitation by MIR pump pulses. In superconducting phase, the transient relative change of reflectivity $\Delta R(\omega, 1.5ps)/R(\omega)$ after excitation of MIR and NIR pump (Fig. 4 (b)) are qualitatively the same, showing a suppression of reflectivity below the static plasmon edge and an enhancement above the edge. Both MIR and NIR pump pulses turn to drive YBCO into a metastable state with JPE at lower energy scale and some incoherent quasiparticles along c-axis, which can be seen in

the inset of Fig. 4 (b). In normal phase, an edge-like shape can be observed in both MIR and NIR pump cases. The effect of the multilayer model used to calculate transient reflectivity actually is the amplification of photo-induced signal. So the calculated pump-induced change will get more significant when the penetration depth of pump pulses gets more inconspicuous than that of probe one (Find in Appendix C). In YBCO, the penetration depths of NIR and MIR pump pulses are 1.3 and 4 respectively (See also in Appendix C). As a result, the calculated photo-induced change is larger in the NIR case even the raw experimental data $\Delta E(t, \tau)/E_{peak}$ are nearly the same, especially in superconducting phase.

It is of great interest to compare the present experimental results with the earlier one reported by Hu et al⁶. The transient reflectivity at maximum NIR pump-induced position (upmost panel of Fig. 2 (d)) is close to their result after excited by 15 μm (MIR) (see Fig. 5j of Ref. 6). Both of those results show that the transient reflectivity is a gentle slope with a slight dip near the static JPE in superconducting state. However, they emphasized that the changes in optical properties are only partial. The observed feature was interpreted as the static JPE being fixed accompanied by a new edge appearing at higher energy scale. In order to explain the edge appearing at higher energy, they assumed non-homogeneous excitations in the pumped regime even after considering the penetration depth mismatch. After fitted by the Bruggeman's effective medium model which can describe a composite or mixed material medium, they implied that a JPE at higher energy scale only exists in 20% volume fraction of the pumped region with the residual pumped portion still remaining in the equilibrium state (see Fig. FS3.1 in supplementary information of Ref. 6). That explanation of those experimental results cannot be supported by our experiments, although the transient reflectivity at maximum NIR pump-induced position looks the same. This is because the transient reflectivity at subsequent time delays depicts a re-emergence and recovery procedure of the static JPE, which indicates that suppression of the static JPE upon exciting is a more plausible explanation. As a result, the Bruggeman's effective medium model is not applicable in superconducting state.

The present work enables us to address two crucial issues with respect to the photo-induced transient superconductivity. The first one is whether or not phonon resonant pumping is essential for the photo-induced effect? In the last few years, mode-selective optical control became particularly attractive because it is argued to base on MIR pumping. The coherent excitation of certain phonon mode can suppress the charge order and simultaneously enhance superconductivity in cuprates. It has motivated many theoretical studies in this direction⁷⁻¹³. Since we find qualita-

tively the same effect by NIR and MIR pumping, phonon pumping could be essentially ruled out. As we emphasized above, the measured raw data are similar in magnitude, the enhanced effect by NIR pumping is mainly due to the difference of penetration depth mismatch. In earlier measurement, it was reported that the photo-induced effect would be reduced when the energy of pump pulse deviates from the phonon mode frequency. Since the penetration depth has a minimum just at the phonon mode, the reduced effect may be related to the enhanced penetration depth when the pump pulse energy is tuned away from the phonon mode.

The second important issue is whether or not the observed phenomenon in the normal state could be attributed to photo-induced transient superconductivity? Our measurement indeed confirms the presence of photo-induced edge-like shape by both NIR and MIR excitations. However, the edge shape is rather weak in the calculated reflectance (Fig. 3 (d)) but can be clearly seen in the relative change of $\Delta R(\omega, \tau)/R$ as shown in Fig. 3 and Fig. 4. The results are similar to the data reported previously^{5,6,26}. However, the interpretation of the new emerging Josephson plasmon edge relies on the analysis based on non-homogeneous excitations and application of Bruggeman's effective medium model, even after taking the penetration depth mismatch of pump and probe pulses into account. A quantitative fit yields roughly 20% of volume fraction in the pumped regime being transformed into transient superconducting component and contributed to the edge like upturn⁶. We elaborated above that our measurement results are not compatible with the non-homogeneous excitations in the superconducting state, then there is no reason that the non-homogeneous excitations could be present in the normal state. On this basis, we can not attribute the observed edge-like shape to the transient superconductivity which gives rise to a JPE in the normal state. The observed upturn should be linked to the quasiparticle excitations, nevertheless its physical origin needs to be further explored.

In summary, we observed a strong pump-induced spectral change in the terahertz frequencies, predominantly near the energy scale of JPE below T_c . The Josephson edge is almost removed upon initial photo excitations, indicating a collapse of superconducting condensate. After a short time delay we observe the reappearance of a JPE at frequency lower than the static JPE, whose feature becomes more pronounced and shifts slightly to higher energy scale with evolution of time delay. Meanwhile, incoherent quasiparticle excitations develop in frequency regime above the static plasma edge. Above T_c , a much smaller pump-induced effect is detected. A weak edge-like shape develops in the reflectance spectrum and sustains even above room temperature. In addition, we find very different time scale for achieving the maximum pump-probe signal between

$T < T_c$ and $T > T_c$. We elaborate that weak edge structure above T_c is unlikely to be explained by the photo-induced transient superconductivity. In addition, there is no substantial difference between the near- and mid-infrared pump cases both in superconducting and normal state, which indicates that phonon pumping as a scenario for the photo excitation effect can be excluded.

ACKNOWLEDGMENTS

This work was supported by National Natural Science Foundation of China (No. 11888101), the National Key Research and Development Program of China (No. 2017YFA0302904, 2016YFA0300902, 2016YFA0300403).

* nlwang@pku.edu.cn

- ¹ K. Tamasaku, Y. Nakamura, and S. Uchida, [Phys. Rev. Lett. **69**, 1455 \(1992\)](#).
- ² S. Uchida, K. Tamasaku, and S. Tajima, [Physical review. B, Condensed matter **53**, 14558 \(1996\)](#).
- ³ C. C. Homes, T. Timusk, R. Liang, D. A. Bonn, and W. N. Hardy, [Phys. Rev. Lett. **71**, 1645 \(1993\)](#).
- ⁴ D. Fausti, R. I. Tobey, N. Dean, S. Kaiser, A. Dienst, M. C. Hoffmann, S. Pyon, T. Takayama, H. Takagi, and A. Cavalleri, [Science **331**, 189 \(2011\)](#).
- ⁵ S. Kaiser, C. R. Hunt, D. Nicoletti, W. Hu, I. Gierz, H. Y. Liu, M. Le Tacon, T. Loew, D. Haug, B. Keimer, and A. Cavalleri, [Phys. Rev. B **89**, 184516 \(2014\)](#).
- ⁶ W. Hu, S. Kaiser, D. Nicoletti, C. R. Hunt, I. Gierz, M. C. Hoffmann, M. Le Tacon, T. Loew, B. Keimer, and A. Cavalleri, [Nature materials **13**, 705 \(2014\)](#).
- ⁷ A. Subedi, A. Cavalleri, and A. Georges, [Phys. Rev. B **89**, 220301\(R\) \(2014\)](#).
- ⁸ S. J. Denny, S. R. Clark, Y. Laplace, A. Cavalleri, and D. Jaksch, [Phys. Rev. Lett. **114**, 137001 \(2015\)](#).
- ⁹ Z. M. Raines, V. Stanev, and V. M. Galitski, [Phys. Rev. B **91**, 184506 \(2015\)](#).
- ¹⁰ M. A. Sentef, A. Tokuno, A. Georges, and C. Kollath, [Phys. Rev. Lett. **118**, 087002 \(2017\)](#).
- ¹¹ J. I. Okamoto, W. Hu, A. Cavalleri, and L. Mathey, [Physical Review B **96**, 1 \(2017\)](#), [arXiv:1706.04554](#).
- ¹² N. Bittner, T. Tohyama, S. Kaiser, and D. Manske, [J. Phys. Soc. Jpn. **88**, 044704 \(2019\)](#).
- ¹³ A. Klein, M. H. Christensen, and R. M. Fernandes, , [arXiv:arXiv:1809.05600v1](#).
- ¹⁴ D. Nicoletti, E. Casandruc, Y. Laplace, V. Khanna, C. R. Hunt, S. Kaiser, S. S. Dhesi, G. D. Gu, J. P. Hill, and A. Cavalleri, [Phys. Rev. B **90**, 1 \(2014\)](#), [arXiv:1404.6796](#).

- ¹⁵ E. Casandruc, D. Nicoletti, S. Rajasekaran, Y. Laplace, V. Khanna, G. D. Gu, J. P. Hill, and A. Cavalleri, [Phys. Rev. B **91**, 174502 \(2015\)](#).
- ¹⁶ S. J. Zhang, Z. X. Wang, L. Y. Shi, T. Lin, M. Y. Zhang, G. D. Gu, T. Dong, and N. L. Wang, [Phys. Rev. B **98**, 020506\(R\) \(2018\)](#).
- ¹⁷ S. J. Zhang, Z. X. Wang, D. Wu, Q. M. Liu, L. Y. Shi, T. Lin, S. L. Li, P. C. Dai, T. Dong, and N. L. Wang, [Phys. Rev. B **98**, 224507 \(2018\)](#).
- ¹⁸ D. Nicoletti, D. Fu, O. Mehio, S. Moore, A. S. Disa, G. D. Gu, and A. Cavalleri, [Phys. Rev. Lett. **121**, 267003 \(2018\)](#).
- ¹⁹ K. A. Cremin, J. Zhang, C. C. Homes, G. D. Gu, Z. Sun, M. M. Fogler, A. J. Millis, D. N. Basov, and R. D. Averitt, [\(2019\), arXiv:1901.10037](#).
- ²⁰ H. Niwa, N. Yoshikawa, K. Tomari, R. Matsunaga, D. Song, H. Eisaki, and R. Shimano, [arXiv:1904.07449v1](#).
- ²¹ S. Tajima, J. Schützmann, S. Miyamoto, I. Terasaki, Y. Sato, and R. Hauff, [Phys. Rev. B **55**, 6051 \(1997\)](#).
- ²² C. Homes, T. Timusk, D. Bonn, R. Liang, and W. Hardy, *Canadian journal of physics* **73**, 663 (1995).
- ²³ R. Mankowsky, A. Subedi, M. Först, S. Mariager, M. Chollet, H. Lemke, J. Robinson, J. Glowia, M. Minitti, A. Frano, *et al.*, *Nature* **516**, 71 (2014).
- ²⁴ R. Comin, R. Sutarto, E. H. d. S. Neto, L. Chauviere, R. Liang, W. N. Hardy, D. A. Bonn, F. He, G. A. Sawatzky, and A. Damascelli, [Science **347**, 1335 \(2015\), 1503.08209](#).
- ²⁵ J. Chang, E. Blackburn, A. T. Holmes, N. B. Christensen, J. Larsen, J. Mesot, R. Liang, D. A. Bonn, W. N. Hardy, A. Watenphul, M. V. Zimmermann, E. M. Forgan, and S. M. Hayden, [Nature Physics **8**, 871 \(2012\)](#).
- ²⁶ C. R. Hunt, D. Nicoletti, S. Kaiser, D. Pröpper, T. Loew, J. Porras, B. Keimer, and A. Cavalleri, [Phys. Rev. B **94**, 224303 \(2016\)](#).
- ²⁷ H. Xiang, L. Guo, H. Li, X. Cui, J. Qian, G. Hussain, Y. Liu, X. Yao, Q. Rao, and Z. Q. Zou, [Scripta Materialia **116**, 36 \(2016\)](#).
- ²⁸ R. Liang, D. A. Bonn, and W. N. Hardy, [Phys. Rev. B **73**, 180505\(R\) \(2006\)](#).
- ²⁹ H. Gao, C. Ren, L. Shan, Y. Wang, Y. Zhang, S. Zhao, X. Yao, and H.-H. Wen, [Phys. Rev. B **74**, 020505 \(2006\)](#).
- ³⁰ S. J. Zhang, Z. X. Wang, T. Dong, and N. L. Wang, [Frontiers of Physics **12**, 127802 \(2017\), arXiv:1708.01991](#).

- ³¹ M. Born and E. Wolf, *Principles of optics: electromagnetic theory of propagation, interference and diffraction of light* (Elsevier, 2013).
- ³² J. Lu, X. Li, Y. Zhang, H. Y. Hwang, B. K. Ofori-Okai, and K. A. Nelson, [Topics in Current Chemistry](#) **376**, 6 (2018).

Appendix A: Experimental details

High-quality single crystals of $\text{YBa}_2\text{Cu}_3\text{O}_{7-\delta}$ were grown by the topseeded solution growth polythermal method using $3\text{BaO}-5\text{CuO}$ solvent with size up to $10\text{ mm}\times 10\text{ mm}\times 6\text{ mm}$ ²⁷. A small piece of single crystal with size about $5\text{ mm}\times 3\text{ mm}\times 2.5\text{ mm}$ was cut from a big crystal and annealed in flowing nitrogen at 520° for 3 weeks. The resulting crystal shows a sharp superconducting transition temperatures near 35 K in the temperature dependent magnetization measurement, as shown in Fig. A1. The measurement indicates that the sample is highly underdoped with oxygen content roughly about 6.45^{28,29}.

The optical reflectance spectra along c-axis from far-infrared (FIR) to ultraviolet region ($15 - 40000\text{ cm}^{-1}$) were measured by Fourier transform infrared spectrometers (FTIR) (Bruker 113v and Vertex 80v) using a in-situ gold and aluminum overcoating technique. With reasonable extrapolations (plotted as green dash lines in Fig. 1 (a)), all optical constants in such a broad range can be obtained through Kramers-Kronig transformation, e.g. complex refractive index.

The equilibrium and photoexcitation induced change of c-axis reflectivity ranging from 10 to 85 cm^{-1} were measured by a time-domain THz spectroscopy system, constructed based on an amplified Ti:sapphire laser system with the pulse duration of 35 fs operating at 1 KHz. NIR/MIR pump beam is generated by a two output optical parametric amplifier seeded by same white light continuum. And the THz probe beam is generated and electro-optic sampling (EOS) by 1-mm-thick ZnTe crystals. The spot sizes of NIR (MIR) pump and probe beam at the sample position are 1.5 mm (1 mm) and 0.63 mm, respectively, which will provide nearly homogeneous excitation. The incident angle of the THz probe beam is 30° with the electric field being perpendicular to the incident plane, i. e. in transverse electric field configuration. Two motorized linear translation stages are used to change the relative time delay of optical pump, THz probe and EOS gate beams. One is on the THz probe beam and the other on the EOS gate beam. Time-domain THz profiles at selective delays are measured by moving only one stage on THz probe beam, which can assure the accuracy of the phase of THz profile. Decay procedure of a specific t of $\Delta\tilde{E}(t, \tau)/E_{peak}$ can be measured by moving both those two stages. Two choppers are used for modulating the THz probe beam (chopper I) and the pump beam (chopper II) independently at 377 Hz, which is in favour of high signal to noise ratio. Static THz reflected electric field is acquired by using only chopper I to modulate the THz probe beam and a lock-in amplifier to read out the balanced EOS diodes. The pump-induced signals are acquired by using only chopper II to modulate pump beam and filtering

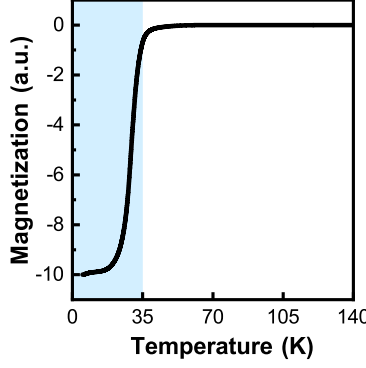


FIG. A1. Temperature-dependent magnetic susceptibility measurement of YBCO.

the pump-induced signal with a lock-in amplifier. More details about difference frequency generation for MIR pump beam and the time-domain THz experimental setup are presented elsewhere³⁰.

Appendix B: Determination of static optical reflectance spectrum in low frequency at 5 K

The optical reflectance spectra in normal state along c-axis of YBCO is almost featureless with only a slight upturn below 100 cm^{-1} , e.g. $R_{40K}(\omega)$, which can be determined by our FTIR spectrometers going down to the lowest measurement frequency 15 cm^{-1} directly, as shown in Fig. 1 (a). At 5 K below T_c , in order to measure Josephson plasmon edge precisely, a terahertz (THz) time-domain spectrometer is used. The reflected THz electric field $\tilde{E}_{5K}(t)$ and $\tilde{E}_{40K}(t)$ (Fig. 1 (b)) are measured by the spectrometer, and the amplitudes of $\tilde{E}_{5K}(\omega)$ and $\tilde{E}_{40K}(\omega)$ can be obtained after doing Fourier transformation (Fig. 1 (c)). Two different calculation methods are used to maintain the accuracy. The first method uses this equation:

$$R_{5K}(\omega) = \frac{|\tilde{E}_{5K}(\omega)|^2}{|\tilde{E}_{40K}(\omega)|^2} \cdot R_{40K}(\omega)$$

to determine $R_{5K}(\omega)$. And the second is based on complex reflected coefficient $\tilde{r}(\omega)$:

$$\tilde{r}_{5K,30^\circ}(\omega) = \frac{\tilde{E}_{5K,30^\circ}(\omega)}{\tilde{E}_{40K,30^\circ}(\omega)} \cdot \tilde{r}_{40K,30^\circ}(\omega),$$

$$R_{5K}(\omega) = |\tilde{r}_{5K,30^\circ}(\omega)|^2$$

where $\tilde{r}_{40K,30^\circ}(\omega)$ is calculated with complex refractive index obtained by FTIR measurements. In the first method, the determination of $R_{5K}(\omega)$ is not sensitive to phase error of reflected electric field, which may be induced by the warming procedure from 5 K to 40 K. In the second one, the incident angle of THz electric field 30° is taken into consideration. $R_{5K}(\omega)$ calculated with those

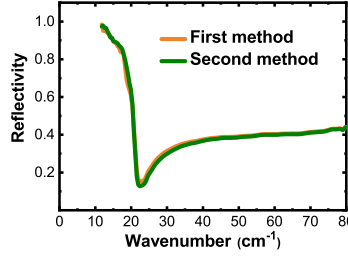


FIG. B1. Reflectivity determined by two different methods.

two methods are almost in coincident with each other, as shown in (Fig. B1). The second method is used in the main text. The optical constants at 5 K is obtained by Kramers-Kronig transformation method, after jointing $R_{5K}(\omega)$ measured by THz spectrometer and FTIR together, in order to avoid the phase sensitivity in THz reflection geometry.

Appendix C: Multilayer model for Transient Optical Constants Calculation

The penetration depth of incident light can be estimated by the imagine part of complex refractive index, obtained by broadband reflectivity spectra of YBCO along c-axis after doing Kramers-Kronig transformation, as shown in Fig. C1 (a). In our pump-probe experiments, two selective wavelength are used to interrogate the pump-induced change of THz regime. MIR pump pulses are tuned to $15 \mu\text{m}$ (667 cm^{-1}) and NIR pump pulses to $1.28 \mu\text{m}$ (7810 cm^{-1}). The penetration depths of those two pump pulses are $4 \mu\text{m}$ and $1.3 \mu\text{m}$ respectively as shown in Fig. C1 (a). In contrast, the penetration depth in THz regime are widely greater than $20 \mu\text{m}$ and even above. That non-negligible mismatch of the penetration depth of pump and probe pulses results in the reflected probe field containing a mixed response of both pumped and unpumped portions of the compound. In order to disentangle those two portions and to obtain the authentic pump-induced change of optical properties, we use a multilayer model assuming that unpumped region lies beneath the pumped region.

When electromagnetic wave, whose wavelength is λ_0 in vacuum, propagates in a non-magnetic layer with a thickness of z , the characteristic matrix $\mathbf{M}(z)$ can be written as

$$\mathbf{M}(z) = \begin{bmatrix} \cos(k_0 \tilde{n} z \cos \theta_0) & -\frac{i}{\tilde{p}} \sin(k_0 \tilde{n} z \cos \theta_0) \\ -i \tilde{p} \sin(k_0 \tilde{n} z \cos \theta_0) & \cos(k_0 \tilde{n} z \cos \theta_0) \end{bmatrix},$$

where θ_0 is the angle of incidence and $k_0 = 2\pi/\lambda_0$. In a stratified medium as a pile of homogeneous

thin films, it is assumed that many homogeneous thin layers with evolving \tilde{n} stack together along the direction of propagation z . If each layer is thin enough, the characteristic matrix of each layer can be written as

$$\mathbf{M}_j = \begin{bmatrix} 1 & -\frac{i}{\tilde{p}_j} k_0 \tilde{n}_j \delta z_j \cos \theta_j \\ -i \tilde{p}_j k_0 \tilde{n}_j \delta z_j \cos \theta_j & 1 \end{bmatrix}.$$

The characteristic matrix of the total medium can be written as a product of the matrices for each layer,

$$\mathbf{M} = \prod_{j=1}^N \mathbf{M}_j = \begin{bmatrix} 1 & -ik_0 B \\ -ik_0 A & 1 \end{bmatrix}, \quad (\text{C1})$$

where

$$A = \sum_{j=1}^N \tilde{p}_j \tilde{n}_j \delta z_j \cos \theta_j, B = \sum_{j=1}^N \frac{\tilde{n}_j}{\tilde{p}_j} \delta z_j \cos \theta_j.$$

Detailed formula derivations can be found in Ref. 31.

For the transverse electric field configuration case in our experiments, $\tilde{p}_j = \tilde{n}_j \cos \theta_j$. In the multilayer model we used, the pumped region is assumed as many homogeneous thin layers stacking together along the direction of propagation, with the pump-induced change of refractive index of each pumped layer evolving in exponential decay, $\tilde{n}(z) = \tilde{n}_0 + \Delta \tilde{n} \cdot e^{-z/l_p}$, where l_p is the penetration depth of pump pulses. The expression for A and B can be rewritten as an integral:

$$A = -ik_0 \int_0^{l_p} dz, B = -ik_0 \int_0^{l_p} \tilde{n}(z)^2 \cos^2 \theta(z) dz$$

Hence the elements of the characteristic matrix are:

$$m_{11} = m_{22} = 1$$

$$m_{12} = -ik_0 l_p$$

$$m_{21} = -ik_0 l_p (\tilde{n}_0^2 + 2(1 - e^{-1}) \tilde{n}_0 \Delta \tilde{n} + \frac{1 - e^{-2}}{2} \Delta \tilde{n}^2 - \sin^2 \theta_0)$$

We denote the vacuum as medium 1, the pumped region of the material as medium 2, and the unpumped region as medium 3. The reflection coefficient acquired by time-domain THz spectroscopy measurements \tilde{r} can be expressed by

$$\tilde{r} = \frac{(m_{11} + m_{12} \tilde{p}_3) \tilde{p}_1 - (m_{21} + m_{22} \tilde{p}_3)}{(m_{11} + m_{12} \tilde{p}_3) \tilde{p}_1 + (m_{21} + m_{22} \tilde{p}_3)}$$

where \tilde{r}_{13} is the equilibrium complex reflection coefficient which can be acquired by FRIT measurements and Kramers-Kronig transformation, and \tilde{r}_{12} is the pump-induced transient complex

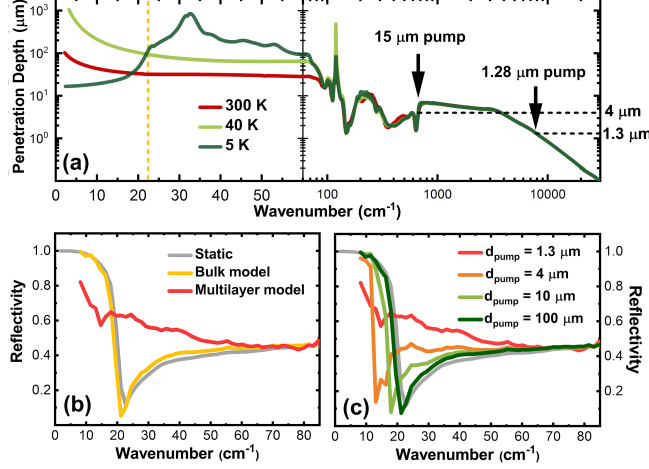


FIG. C1. A multilayer model should be used to obtain the authentic pump-induced change of optical properties, for the non-neglecting penetration depth difference between pump and probe pulse. (a) the penetration depth of incident light estimated by the imagine part of complex refractive index. (b) the transient reflectivity calculates with bulk model and multilayer model. (c) The pump-induced change gets weaker when the penetration depth of pump l_p gets deeper, and will be in coincident with bulk model if we assume l_p is comparable with the penetration depth of probe pulses.

reflection coefficient considering the penetration depth mismatch which is waiting for the following calculation, $\tilde{p}_1 = \cos\theta_0$ and $\tilde{p}_3 = \frac{1-\tilde{r}_{13}}{1+\tilde{r}_{13}}\cos\theta_0$. Hence, $\Delta\tilde{n}$ can be solved as an unknown of a quadratic equation shown below

$$\frac{1-e^{-2}}{2}ik_0l_p \cdot \Delta\tilde{n}^2 + 2(1-e^{-1})ik_0l_p\tilde{n}_0 \cdot \Delta\tilde{n} + (1-ik_0l_p\tilde{p}_3)\tilde{p}_1 \frac{1-\tilde{r}}{1+\tilde{r}} + (ik_0l_p\tilde{n}_0^2 - ik_0l_p\sin^2\theta_0 - \tilde{p}_3) = 0.$$

There may exist two roots for the quadratic equation according to the quadratic formula. The way to pick a reasonable solution is to maintain the real part of $\tilde{n}' = \tilde{n}_0 + \Delta\tilde{n}$ positive, for the calculated results should keep in line with the definition of physical quantities.

To check the reasonability of the multilayer model, we now compare the calculated results with different l_p . If the penetration depth mismatch between pump and probe pulses is neglected, the probed region will be seen as being uniformly pumped, which is defined as “bulk model”. The transient reflectivity can be calculated using the second method in Appendix B:

$$\begin{aligned}\tilde{r}'(\omega, \tau) &= \frac{\tilde{E}'(\omega, \tau)}{\tilde{E}_{5K}(\omega)} \cdot \tilde{r}_{5K}(\omega), \\ R'(\omega, \tau) &= |\tilde{r}'(\omega, \tau)|^2\end{aligned}$$

where $\tilde{E}'(\omega, \tau)$ is the Fourier transformation of $\tilde{E}'(t, \tau) = \tilde{E}_{5K}(t) + \Delta\tilde{E}(t, \tau)$.

Figure C1 (b) shows the calculated transient reflectivity at 9 ps after the excitation of 1.28 μm pump by a fluence of 1 mJ/cm^2 using bulk model and multilayer model. The pump-induced change, i.e. reflectivity being suppressed below the static edge and enhanced at higher energy scale. The pump-induced effects will get weaker if we assume a deeper penetration of pump pulses, as shown in Fig. C1 (c). When l_p is assumed to be 100 μm , which is comparable with the penetration depth of probe, the results calculated using multilayer model seems nearly the same with that using bulk model. That validates the application of the multilayer model we use.

Appendix D: Determination of the relative phase

As presented in Appendix A, two choppers work independently in the time-domain THz spectroscopy system. So the relative phase between static reflected electric field $\tilde{E}_0(t)$ and the pump-induced change at selective time delay $\Delta\tilde{E}(t, \tau)$ is unable to know directly. To determine the relative phase, we use the definition of pump-induced change:

$$\Delta\tilde{E}(t, \tau) = \tilde{E}_{pumped}(t, \tau) - \tilde{E}_0(t)$$

where $\tilde{E}_{pumped}(t, \tau)$ is measured in the same way as $\tilde{E}_0(t)$ but with pump light shedding on the sample. The relative phase of $\Delta\tilde{E}(t, \tau)$ can be determined by that method in superconducting phase, for the pump-induced signal is large enough. But for $\Delta\tilde{E}(t, \tau)$ in normal phase, $\tilde{E}_{pumped}(t, \tau) - \tilde{E}_0(t)$ may be disguised by fluctuations at THz peak position.

A double modulation technique is further used for determining the relative phase of $\Delta\tilde{E}(t, \tau)$ in normal state of YBCO. Two choppers is directly triggered by the Ti:sapphire laser system, whose repetition rate is 1 KHz. Pump beam and THz probe beam are modulated at 250 and 500 Hz respectively by those choppers. A multichannel high-speed data acquisition card (DAQ) is used to read out the electro-optic sampling balanced detectors³². In that configuration, there will be four different cases (A, B, C, D) if the phase of the two choppers are correctly set, as shown in Fig. D1. Signals can be read out by DAQ only in case A and C, i.e. $\tilde{E}_{pumped}(t, \tau)$ and $\tilde{E}_0(t)$, every four pulses. To distinguish those two different signals read out by DAQ, the phase between chopper I and chopper II should be fixed using a reference, on which difference between $\tilde{E}_{pumped}(t, \tau)$ and $\tilde{E}_0(t)$ is significant enough to be distinguished.

For YBCO at 5 K, the difference between $\tilde{E}_{pumped}(t, \tau)$ and $\tilde{E}_0(t)$, i.e. $\Delta\tilde{E}(t, \tau)$, is over 5% of

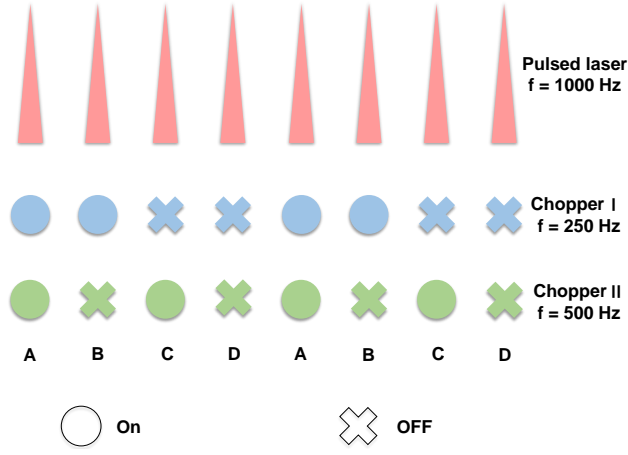


FIG. D1. Schematic diagram of double modulation technique. "On" represents the light shedding on the sample and "Off" means the light is blocked by the blades of choppers.

E_{peak} , which can be resolved by the DAQ detection method even the signal to noise ratio is relatively miserable. According to the results measured by the lock-in method presented in Appendix A, the phase of chopper I and chopper II can be fixed to meet the specific condition illustrated in Fig. D1. Then, the phase of $\Delta\tilde{E}(t, \tau)$ in normal state of YBCO can be determined.